Systematic study of proton radioactivity based on the double-folding potential model*

Hai-Tao Yang (杨海涛)[1†] Zhong-Xia Zhao (赵仲霞)[1] Xiao-Pan Li (李孝攀)[1] Yu-Hui Luo (罗玉辉)[1]
Xun Xue (薛迅)[1,3] Xiao-Jun Bao (包小军)[2‡]

[1]Department of Physics, Zhaotong University, Zhaotong 657000, China
[2]Department of Physics, Collaborative Innovation Center for Quantum Effects, and Key Laboratory of Low Dimensional Quantum Structures and Quantum Control of Ministry of Education, Hunan Normal University, Changsha 410081, China
[3]Department of Physics, East China Normal University, Shanghai 200241, China

Abstract: We study proton radioactivity in proton-rich nuclei with $53 \leqslant Z \leqslant 83$ within a semi-microscopic framework in which the emitted proton is described by a finite-size density distribution. Two proton-density prescriptions are considered, namely, Gaussian and Fermi profiles. When microscopic spectroscopic factors are combined with a double-folding potential based on finite-size proton and daughter densities, the Fermi-density prescription yields the best overall agreement with the experimental results, reducing the global root-mean-square deviation of $\log_{10} T_{1/2}$ to $\sigma = 0.37$. In addition, a modified universal decay law that embeds the same spectroscopic factors yields an even smaller deviation, $\sigma = 0.28$, providing a high-precision global description of proton-radioactivity half-lives. We construct the proton–daughter interaction by folding a Skyrme-type effective nucleon–nucleon interaction with finite-size proton densities and spherical daughter densities and evaluate proton-emission half-lives within the Wentzel–Kramers–Brillouin approximation for 39 known proton emitters in this region. State-dependent spectroscopic factors S_p^{QYB} and S_p^{ZHF} obtained from relativistic mean-field plus Bardeen–Cooper–Schrieffer calculations are employed to account for proton preformation. Subsequently, we compare the calculated half-lives with experimental data and analyze the residuals by grouping them according to the minimum orbital angular momentum and based on whether the decay proceeds from the ground or isomeric state. Finally, we extend the universal decay law for proton emission (UDLP) by including an explicit spectroscopic-factor term, obtaining a modified formula (MUDLP) that provides a compact global parametrization of experimental proton-radioactivity half-lives. Using the best-performing semi-microscopic prescription together with the MUDLP parametrization, we provide conditional half-life estimates for several candidate proton emitters near the proton drip line, where the input Q_p values are taken from AME2020. These results provide quantitative reference values for future experimental searches for new proton-radioactive nuclei.

Keywords: proton radioactivity, double-folding potential, spectroscopic (preformation) factor, UDLP

DOI: 10.1088/1674-1137/ae4a90 **CSTR:** 32044.14.ChinesePhysicsC.50054108

I. INTRODUCTION

Proton radioactivity is one of the most important decay modes of proton-rich nuclei far from the β-stability line, and it sets stringent limits on the production of increasingly exotic systems. It was first observed in 1970 in an isomeric state of ^{53}Co [1, 2]. With the rapid development of radioactive-ion-beam facilities, proton emissions have since been identified from ground and low-lying isomeric states of parent nuclei in the mass region A=110−180 [3]. This decay mode is characteristic of odd-Z nuclei located beyond the proton drip line and provides a powerful probe into the nuclear structure, including the shell structure, coupling between bound and unbound states, and spectroscopic-factor properties of exotic systems [4−6]. The emission process can be treated as quantum tunneling through a potential barrier, in close analogy to α decay. Numerous theoretical frameworks have been developed to describe proton radioactivity, such as the generalized liquid-drop model [5, 6], two-po-

Received 10 December 2025; Accepted 26 February 2026; Accepted manuscript online 27 February 2026

* Supported by the Natural Science Foundation of China (12175064, 12363003, 12365007, U2167203), the Special Basic Cooperative Research Programs of Yunnan Provincial Undergraduate Universities' Association (202101BA070001-144), Hunan Outstanding Youth Science Foundation (2022JJ10031)

† E-mail: yanghaitao205@163.com
‡ E-mail: baoxiaojun@hunnu.edu.cn

tential approach [7−10], distorted-wave Born approximation [11], coupled-channels methods [12−14], unified fission model [15, 16], Coulomb-and-proximity-potential model [3], single-folding models [17−20], and Gamow-like model [21−23]. In these approaches, the barrier includes Coulomb, nuclear, and centrifugal contributions. Although the Coulomb and centrifugal parts are straightforward to construct, the nuclear potential can be modeled in various ways, including analytical expressions [7, 24], proximity potentials [25, 26], and folding potentials [20, 27]. The choice of nuclear potential is key to improving the accuracy of half-life predictions. Consequently, models based on different nuclear potentials can exhibit significantly different predictive performance. For example, even within the same theoretical framework, such as the Coulomb-and-proximity-potential model, different versions of the proximity-potential formula can lead to considerable differences in predictive power [28]. Inspired by our previous work on α decay, [29] where a double-folding potential model (DPM) based on a Skyrme-type effective nucleon–nucleon interaction (neglecting momentum and spin dependence) successfully reproduced experimental half-lives, we extend this approach to investigate proton radioactivity. Applying the same microscopic framework is a natural extension because both α decay and proton emission are essentially quantum tunneling processes. Traditionally, the interaction potential between the emitted proton and the daughter nucleus has often been calculated within a single-folding approximation, wherein the proton is treated as a point-like particle. In contrast, reaction and scattering studies of proton–nucleus systems commonly describe both participants by finite-size density distributions. For example, Patterson and Peterson employed a Gaussian charge distribution for the proton to unfold its charge structure from measured nuclear charge distributions, providing standard parameter sets for use in impulse-approximation descriptions of hadron–nucleus reactions [30]. Spin-dependent Glauber-model calculations, such as those implemented in the SDGMPS code, adopt Gaussian proton charge densities together with phenomenological or microscopic nuclear matter distributions as basic inputs to describe intermediate-energy proton–nucleus elastic scattering and constrain root mean square (RMS) radii [31]. Double-folding optical potentials frequently combine Woods–Saxon–type proton densities with nucleon densities from relativistic Hartree–Bogoliubov calculations [32]. Similar strategies have been used in decay models, where double-folding an effective nucleon–nucleon interaction with Gaussian cluster densities provides a unified framework for α decay, heavy-cluster radioactivity, and, more recently, two-proton radioactivity [33]. These precedents show that representing both the target and projectile (or emitted cluster) by finite-size densities is a natural and widely used choice in folding descriptions of proton–daughter interaction. Motivated by these developments, this work presents the emitted proton by a finite-size density distribution, considering both two-parameter Fermi and Gaussian profiles when constructing the proton–daughter interaction within a double-folding potential model based on a Skyrme-type effective nucleon–nucleon interaction.

In addition, the spectroscopic factor, which is often referred to as the preformation factor, is a key quantity governing the accuracy of proton radioactivity half-life calculations. Microscopically, it can be considered the probability that a blocked proton in a given orbital of the parent nucleus is transferred to the corresponding empty orbital in the daughter nucleus [8]. Currently, two major categories of methods have been developed for its determination: microscopic and phenomenological approaches. Microscopic methods are independent of the barrier-penetration model and derived directly from nuclear-structure theories. They are typically based on various mean-field frameworks combined with pairing correlations, such as the relativistic mean-field theory with the Bardeen–Cooper–Schrieffer method (RMF+BCS) [6, 20, 27, 34], relativistic continuum Hartree–Bogoliubov theory [35], and covariant density functional theory combined with BCS [36]. These approaches can incorporate shell effects, deformation, and quantum mixing, providing a more fundamental description of the spectroscopic factor. In contrast, phenomenological methods extract the spectroscopic factor from the ratio of theoretical to experimental half-lives or propose empirical expressions that embed nuclear-structure information. Representative examples include the analytic expression proposed by Chen *et al*. as a function of the cube root of the daughter mass number [7] and the formula established by Zhang *et al*., which links the spectroscopic factor to the quadrupole deformation parameter within the deformed two-potential approach [8]. These phenomenological treatments significantly improve the reproduction of experimental data, although their results exhibit a certain degree of model dependence. In general, microscopic methods provide greater physical interpretability, while phenomenological approaches are tailored to enhance predictive accuracy. In this study, we employ spectroscopic factors calculated microscopically within the RMF+BCS framework by Zhang *et al*. [6] and Qian *et al*. [20] as input quantities in the evaluation of proton-radioactivity half-lives to assess the intrinsic reliability of the DPM.

Analytic expressions provide a compact and complementary route for evaluating proton-emission half-lives alongside barrier-penetration models. Building on the Geiger–Nuttall law, a number of empirical or analytic formulations have been proposed for proton radioactivity. Among them, the universal decay law for proton emission (UDLP) proposed by Qi *et al*. [5] has been widely used as a baseline in systematic studies and as a common

reference for comparison with newer formulas and models [23, 37]. A key refinement for improving global proton-radioactivity systematics is to embed explicit nuclear-structure information, especially the spectroscopic (preformation) factor, directly into the analytic description. For spherical proton emitters, Zhang and Dong demonstrated that incorporating a spectroscopic (preformation) factor from microscopic RMF+BCS calculations into the half-life formula significantly improves agreement with the experimental results relative to formulas that neglect preformation effects [38]. Similarly, complementary empirical systematics indicate that half-life formulas embedding the spectroscopic-factor and deformation dependences attain smaller RMS deviations than those of structure-agnostic expressions that depend only on Q values and global Z, A systematics, underscoring the practical benefit of incorporating nuclear-structure information into analytic descriptions [38, 39]. Motivated by these developments, in addition to our double-folding-potential calculations, we adopt the UDLP as a reference analytic scaffold and extend it by an explicit spectroscopic-factor term, using values taken from published RMF+BCS calculations [6, 20] to improve its performance in describing proton-radioactivity half-lives.

Throughout this study, the proton-decay energy Q_p is taken from the most recent atomic-mass evaluation (AME2020). Therefore, the present calculations are intended for a systematic evaluation and benchmarking of the barrier description and microscopic spectroscopic factors for known (or mass-evaluated) 1p emitters, and the reported half-lives should be interpreted as conditional on the adopted Q_p. A fully predictive description for truly unknown emitters would require theoretical Q_p values (e.g., from global mass models) or microscopic resonance approaches that determine the resonance energy and width simultaneously, which is beyond the scope of this study.

The remainder of this paper is organized as follows. Section II outlines the theoretical framework. Section III presents numerical results and discussions. Section IV summarizes our conclusions.

II. THEORETICAL FRAMEWORK

A. Double-folding potential model

The proton radioactivity half-lives can be calculated by

$$T_{1/2} = \frac{\ln 2}{\nu_0 P S_p}, \tag{1}$$

where P is the barrier penetration probability, ν_0 denotes the assault frequency of the proton inside the parent nucleus, and S_p represents the spectroscopic factor of the emitted proton-daughter system. In the microscopic RMF+BCS description, the proton spectroscopic factor S_p is taken as the vacancy probability of the decaying proton orbital in the daughter nucleus. Following Refs. [6, 20], one can write $S_p = u_j^2$, where u_j^2 represents the probability that the specific orbit associated with the emitted proton is empty in the daughter nucleus. In this study, we directly adopt the state-dependent RMF+BCS spectroscopic factors from Zhang *et al.* (S_p^{ZHF}) and Qian *et al.* (S_p^{QYB}), and all numerical values used are explicitly listed in Table 1. The penetrability P is calculated within the Wentzel-Kramers-Brillouin (WKB) approximation and reads

$$P = \exp\left[-\frac{2}{\hbar}\int_{R_{\mathrm{in}}}^{R_{\mathrm{out}}} \sqrt{2\mu(V(r)-Q_p)}\,\mathrm{d}r\right], \tag{2}$$

where Q_p is the release energy, and μ represents the reduced mass of the system. $V(r)$ denotes the total interaction potential between the proton and the daughter nucleus. The classical turning points R_{in} and R_{out} are given by [40]

$$R_{\mathrm{in}} = R_1 + R_2, \tag{3}$$

and

$$R_{\mathrm{out}} = \frac{Z_1 Z_2 e^2}{2Q_p} + \sqrt{\left(\frac{Z_1 Z_2 e^2}{2Q_p}\right)^2 + \frac{\hbar^2 l(l+1)}{2\mu Q_p}}, \tag{4}$$

where R_1 and R_2 are the equivalent radii of the proton and the daughter nucleus, respectively. The equivalent radii of the parent ($i=0$), emitted proton ($i=1$), and daughter nucleus ($i=2$) are taken as[40]

$$R_i = 1.28A_i^{1/3} - 0.76 + 0.8A_i^{-1/3} \quad (\mathrm{fm}), \quad i = 0,1,2. \tag{5}$$

The total interaction potential $V(r)$ consists of the Coulomb, nuclear, and centrifugal parts and is given by

$$V(r) = V_C(r) + V_N(r) + \frac{\hbar^2 l(l+1)}{2\mu r^2}, \tag{6}$$

where l presents the angular momentum, which can be obtained by considering the spin-parity conservation of the decay process. The nuclear potential $V_N(r)$ between the proton and daughter nuclei is obtained using a double-folding formalism with a Skyrme-type effective nucleon-nucleon interaction by ignoring the momentum and spin dependence, as in Refs. [41, 42].

Table 1. Experimental proton-emission half-lives and DPM results using RMF+BCS spectroscopic factors $S_p^{\rm QYB}$ and $S_p^{\rm ZHF}$. The columns $S_p^{\rm QYB}$ and $S_p^{\rm ZHF}$ are adopted from RMF+BCS calculations in Refs. [6, 20], respectively. The calculated $\log_{10}T_{1/2}$ values are listed for two proton-density prescriptions (Gaussian and Fermi) and the baseline choice $S_p = 1$; UDLP and MUDLP results are included for comparison.

Nucleus	Q_p/MeV	l	$S_p^{\rm QYB}$	$S_p^{\rm ZHF}$	$\log_{10}T_{1/2}$/s									
					Expt	$S_p=1$			$S_p^{\rm QYB}$			$S_p^{\rm ZHF}$		
						Gaussian	Fermi	UDLP	Gaussian	Fermi	MUDLP	Gaussian	Fermi	MUDLP
^{109}I	0.83	2	0.44	0.73	−4.03	−4.00	−4.40	−3.54	−4.39	−4.04	−3.34	−4.62	−4.27	−3.89
^{112}Cs	0.82	2	0.46	0.37	−3.31	−3.11	−3.56	−2.81	−3.53	−3.23	−2.61	−3.43	−3.13	−2.78
^{113}Cs	0.98	2	0.45	0.37	−4.77	−5.31	−5.73	−4.75	−5.72	−5.38	−4.68	−5.64	−5.30	−5.00
^{117}La	0.83	2	0.18	0.31	−1.66	−2.55	−3.02	−2.38	−2.57	−2.29	−1.77	−2.80	−2.52	−2.23
^{121}Pr	0.90	2	0.11	0.12	−1.92	−2.89	−3.39	−2.73	−2.68	−2.41	−1.94	−2.73	−2.47	−2.24
^{130}Eu	1.03	2	0.67	0.82	−3.00	−3.31	−3.84	−3.20	−3.89	−3.66	−3.30	−3.98	−3.75	−3.63
^{131}Eu	0.96	2	0.65	0.03	−1.70	−2.41	−2.94	−2.41	−2.99	−2.75	−2.44	−1.63	−1.40	−1.29
^{135}Tb	1.20	3	0.52	0.03	−3.00	−3.73	−4.53	−3.71	−4.21	−4.24	−3.84	−2.94	−2.98	−2.82
^{140}Ho	1.10	3	0.75	0.95	−2.22	−2.04	−2.85	−2.27	−2.67	−2.73	−2.47	−2.78	−2.83	−2.72
^{141}Ho	1.19	3	0.80	0.01	−2.39	−3.09	−3.89	−3.19	−3.75	−3.79	−3.50	−1.75	−1.79	−1.69
^{141}Ho$^{\rm m}$	1.26	0	0.72	0.05	−5.14	−5.71	−5.90	−5.29	−6.32	−5.76	−5.56	−5.15	−4.58	−4.76
^{145}Tm	1.75	5	0.62	0.58	−5.50	−4.77	−5.95	−4.70	−5.32	−5.74	−5.24	−5.29	−5.72	−5.42
^{146}Tm	0.90	0	0.75	0.96	−0.81	−0.40	−0.69	−0.66	−1.04	−0.56	−0.62	−1.15	−0.67	−0.81
^{146}Tm$^{\rm m}$	1.21	5	0.75	0.96	−1.14	−0.26	−1.41	−0.79	−0.90	−1.29	−1.12	−1.01	−1.40	−1.20
^{147}Tm	1.07	5	0.72	0.58	0.59	1.44	0.29	0.69	0.82	0.43	0.49	0.92	0.52	0.71
^{147}Tm$^{\rm m}$	1.13	2	0.71	0.95	−3.44	−2.72	−3.28	−2.84	−3.33	−3.13	−3.02	−3.46	−3.26	−3.34
^{150}Lu	1.29	5	0.52	0.50	−1.35	−0.49	−1.64	−1.04	−0.96	−1.35	−1.25	−0.95	−1.33	−1.21
^{150}Lu$^{\rm m}$	1.31	2	0.74	0.86	−4.40	−4.01	−4.58	−4.02	−4.63	−4.45	−4.34	−4.70	−4.52	−4.65
^{151}Lu	1.26	5	0.52	0.49	−0.90	−0.19	−1.35	−0.78	−0.66	−1.07	−0.97	−0.64	−1.04	−0.90
^{151}Lu$^{\rm m}$	1.32	2	0.75	0.86	−4.80	−4.12	−4.68	−4.12	−4.75	−4.56	−4.45	−4.81	−4.62	−4.77
^{155}Ta	1.47	5	0.38	0.42	−2.50	−1.74	−2.92	−2.18	−2.08	−2.50	−2.36	−2.12	−2.55	−2.44
^{156}Ta	1.04	2	0.68	0.76	−0.83	−0.20	−0.82	−0.68	−0.79	−0.65	−0.73	−0.84	−0.70	−0.81
^{156}Ta$^{\rm m}$	1.13	5	0.41	0.49	0.93	1.84	0.69	0.98	1.48	1.08	1.01	1.39	0.99	1.08
^{157}Ta	0.95	0	0.91	0.80	−0.53	0.27	−0.06	−0.13	−0.44	−0.02	−0.20	−0.39	0.04	−0.16
^{159}Re	1.82	5	0.23	0.31	−4.68	−4.00	−5.19	−4.15	−4.12	−4.55	−4.29	−4.25	−4.68	−4.56
^{160}Re	1.28	2	0.67	0.51	−3.16	−2.62	−3.24	−2.86	−3.20	−3.06	−3.09	−3.08	−2.94	−3.13
^{161}Re	1.22	0	0.91	0.89	−3.36	−2.84	−3.18	−2.94	−3.56	−3.14	−3.25	−3.55	−3.13	−3.42
^{161}Re$^{\rm m}$	1.34	5	0.23	0.29	−0.68	−0.09	−1.28	−0.75	−0.20	−0.63	−0.62	−0.31	−0.74	−0.67
^{164}Ir	1.84	5	0.17	0.19	−3.95	−3.78	−4.98	−4.02	−3.77	−4.20	−4.03	−3.82	−4.25	−4.20
^{165}Ir$^{\rm m}$	1.73	5	0.17	0.19	−3.43	−2.99	−4.18	−3.32	−2.98	−3.41	−3.29	−3.02	−3.45	−3.41
^{166}Ir	1.17	2	0.36	0.42	−0.82	−0.74	−1.39	−1.25	−1.06	−0.95	−1.13	−1.12	−1.00	−1.23
^{166}Ir$^{\rm m}$	1.35	5	0.19	0.19	−0.08	0.32	−0.87	−0.44	0.28	−0.15	−0.24	0.29	−0.15	−0.14
^{167}Ir	1.09	0	0.89	0.91	−1.12	−0.55	−0.92	−0.96	−1.26	−0.87	−1.14	−1.27	−0.88	−1.20
^{167}Ir$^{\rm m}$	1.26	5	0.17	0.18	0.84	1.25	0.05	0.36	1.26	0.83	0.69	1.23	0.79	0.79
^{171}Au	1.46	0	0.87	0.85	−4.65	−4.31	−4.67	−4.34	−5.01	−4.61	−4.79	−4.99	−4.59	−5.02
^{171}Au$^{\rm m}$	1.72	5	0.07	0.09	−2.59	−2.51	−3.71	−2.96	−2.08	−2.53	−2.50	−2.21	−2.65	−2.68
^{177}Tl	1.17	0	0.50	0.73	−1.17	−0.47	−0.89	−0.99	−0.92	−0.59	−0.97	−1.09	−0.75	−1.17
^{177}Tl$^{\rm m}$	1.97	5	0.02	0.02	−3.35	−3.83	−5.03	−4.16	−2.93	−3.38	−3.34	−2.93	−3.38	−3.46
^{185}Bi$^{\rm m}$	1.63	0	0.03	0.01	−4.19	−4.73	−5.09	−4.83	−4.00	−3.60	−3.94	−3.53	−3.14	−3.72

$$V_N(r) = C_0 \left\{ \frac{F_{\rm in} - F_{\rm ex}}{\rho_{00}} \left(\int \rho_1^2(R)\rho_2(R-r)\,{\rm d}R + \int \rho_1(R)\rho_2^2(R-r)\,{\rm d}R \right) + F_{\rm ex} \int \rho_1(R)\rho_2(R-r)\,{\rm d}R \right\}. \quad (7)$$

with

$$F_{\rm in,ex} = f_{\rm in,ex} + f'_{\rm in,ex} \frac{N_1 - Z_1}{A_1} \frac{N_2 - Z_2}{A_2}, \quad (8)$$

where $Z_{1,2}$, $N_{1,2}$, and $A_{1,2}$ represent the proton, neutron, and mass numbers of the emitted particle and daughter nucleus, respectively. The parameters in Eqs. (7)–(8) are adopted from Ref. [42] with the values: $C_0 = 300$ MeV$\cdot$fm^3, $f_{\rm in} = 0.09$, $f_{\rm ex} = -2.59$, $f'_{\rm in} = 0.42$, $f'_{\rm ex} = 0.54$, and $\rho_{00} = 0.17\,{\rm fm}^{-3}$. The folding barrier (and hence the penetrability) is evaluated within a standard WKB treatment using a nonrelativistic Skyrme-type effective interaction, whereas the RMF+BCS spectroscopic factor S_p is introduced separately as an independent microscopic structure factor. $\rho_1(R)$ represents an effective finite-size smearing profile for the emitted proton, while $\rho_2(R)$ represents the matter density distribution of the daughter nucleus. Following Ref. [32], we adopt a two-parameter Fermi form for the proton profile and daughter density:

$$\rho_1(R) = \frac{\rho_{00}}{1 + \exp((R - R_1)/a_1)}, \quad (9)$$

$$\rho_2(R) = \frac{\rho_{00}}{1 + \exp((|R - r| - R_2)/a_2)}, \quad (10)$$

Here, $\rho_{00} = 0.17$ fm^{-3} is used consistently with the saturation-density parameter entering the effective interaction in Eq. (7), and it is utilized as a fixed convention in the adopted Fermi profiles. The radii R_1 and R_2 are considered as the equivalent radii defined in Eq. (5), while the diffuseness parameters are fixed at $a_1 = a_2 = 0.54$ fm [20]. Further, we tested $a_1 = a_2 = 0.52$ fm and found that $a_1 = a_2 = 0.54$ fm yields a smaller overall RMS deviation for the benchmark set; therefore, $a_1 = a_2 = 0.54$ fm is adopted. However, for light spherical nuclei, a Gaussian form is tested for the proton profile [30]:

$$\rho_1(R) = \rho_{0p} \exp\left[-(R/a_p)^2\right], \quad (11)$$

with $a_p = 0.704$ fm [30], where ρ_{0p} is fixed by the unit normalization $4\pi \int_0^\infty \rho_1(R) R^2\,{\rm d}R = 1$.

The Coulomb potential is taken in the uniformly charged-sphere form used in the DPM of Ref. [43].

$$V_C(r) = \begin{cases} \dfrac{Z_1 Z_2 e^2}{r}, & r > R_c, \\ \dfrac{Z_1 Z_2 e^2}{2R_c}\left[3 - \left(\dfrac{r}{R_c}\right)^2\right], & r \leqslant R_c. \end{cases} \quad (12)$$

where $R_c = R_1 + R_2$, and Z_1 and Z_2 are the charge numbers of the proton and daughter nucleus, respectively. The assault frequency ν_0 is evaluated within a quantum-mechanical approach as [40]

$$\nu_0 = \frac{\omega}{2\pi} = \frac{(G + \frac{3}{2})\hbar}{1.2\pi\mu R_0^2}, \quad (13)$$

where R_0 represents the effective radius of the parent nucleus, G is the principal quantum number, and μ is the reduced mass of the emitted particle and daughter nuclei system. For details, see Ref. [40].

B. Empirical formulas for proton radioactivity

The present work is based on the UDLP, which was derived by Qi *et al.* from the microscopic mechanism of charged-particle emission. It is expressed as [5]

$$\log_{10} T_{1/2} = a\chi' + b\rho' + c + d\frac{\ell(\ell+1)}{\rho'}, \quad (14)$$

where $\chi' = Z_d \sqrt{\dfrac{A_d}{(A_d+1)Q_p}}$, and $\rho' = \sqrt{\dfrac{A_d Z_d \left(A_d^{1/3}+1\right)}{A_d+1}}$. To improve the predictive performance for proton radioactivity, analogous to the approach of Zhang *et al.* [38], we incorporate an explicit spectroscopic (preformation) factor into the UDLP. The resulting expression is

$$\log_{10} T_{1/2} = a\chi' + b\rho' + c + d\frac{\ell(\ell+1)}{\rho'} - \log S_p. \quad (15)$$

where a, b, c, and d are adjustable parameters, whose values are determined by fitting experimental data of proton radioactivity.

III. RESULTS AND DISCUSSION

In our previous study, a DPM based on a Skyrme-type effective nucleon–nucleon interaction, in which momentum- and spin-dependent terms are neglected, was successfully applied to nuclear α decay and found to reproduce experimental half-lives with good accuracy. In the present study, motivated by the fact that both proton radioactivity and α decay originate from the same quantum-tunneling mechanism, we extended the DPM framework to investigate nuclear proton radioactivity. In the description of radioactive decay, the choice of the interaction potential between the emitted particle and

daughter nucleus is crucial for improving the accuracy of half-life calculations [7]. However, within a double-folding framework, the adopted density distribution of the emitted particle also modifies the nuclear potential and affects the predicted decay half-lives. Therefore, in this study, we compute proton-emission half-lives for 39 proton emitters with $53 \leqslant Z \leqslant 83$ using the DPM with two different prescriptions for the proton density: a Gaussian profile and a two-parameter Fermi profile. The lower bound $Z = 53$ is selected for the benchmark set of established proton emitters with measured half-lives, for which the microscopic RMF+BCS spectroscopic factors S_p tabulated in Ref. [6] are available in a consistent manner. For completeness, we also consider a few candidate nuclei with $Z \leqslant 52$ (e.g., Sb isotopes) in the subsequent conditional predictions; these cases are not included in the global systematics or RMS evaluation. A small number of additional candidate nuclei (such as ^{108}I, ^{144}Tm, ^{159}Re$^{\mathrm{m}}$, and ^{170}Au$^{\mathrm{m}}$) are not included because we require a uniform use of the state-dependent preformation factors tabulated by Zhang *et al*. in the subsequent analysis, and these nuclei do not have corresponding S_p values in that table (Ref. [6]). To assess the reliability of our calculations, we systematically compare the theoretical results with the available experimental data. The experimental proton-emission half-lives and spin–parity assignments of the parent and daughter nuclei are obtained from the latest evaluated nuclear-structure compilation NUBASE2020 [44], while the Q_p values are adopted from the most recent atomic-mass evaluation AME2020 [45]. Consequently, the calculated (and extrapolated) half-lives in this study should be viewed as conditional estimates given the adopted Q_p values, and any future revisions of Q_p are expected to directly propagate into the predicted $\log T_{1/2}$.

In the systematic calculations, the daughter nuclei are treated within the spherical approximation, *i.e.*, spherical radii/densities are adopted to construct the interaction barrier. However, for axially deformed nuclei, the nuclear radius and barrier profile become orientation dependent, leading to an angle-dependent penetrability $P(\theta)$. Previous studies have shown that deformation and barrier orientation may thin the barrier for favorable directions, thus enhancing the penetrability, which results in shorter half-lives than the spherical estimate, especially for well-deformed emitters [3, 46, 47]. The quantitative impact of deformation on global agreement (*e.g.*, RMS deviation) depends on the adopted deformation parameters, treatment of orientation effects, and consistency between the potential model and structure input. Since the main purpose of this study is to establish a uniform baseline for global systematics, the deformation degrees of freedom are not explicitly included for all nuclei at the present stage. Extending the present double-folding framework to deformed densities and/or orientation-averaged penetrabilities will be an important subject of our future work.

We first consider a baseline calculation with the spectroscopic factor fixed to unity ($S_p = 1$), neglecting preformation effects. Within the DPM framework, we calculate proton radioactivity half-lives using the two choices of emitted-proton density, Gaussian and Fermi. The corresponding results are listed in columns 7 and 8 of Table 1. Overall, the half-lives obtained with both density prescriptions are in reasonable agreement with the experiment. To quantify the global performance of the model, we evaluate the RMS deviation between theoretical and experimental half-lives according to

$$\sigma = \sqrt{\frac{1}{N}\sum_{i=1}^{N}\left(\log_{10} T^{\mathrm{cal}}_{1/2,i} - \log_{10} T^{\mathrm{exp}}_{1/2,i}\right)^2}. \tag{16}$$

A comparative analysis of the deviations shows that, when the emitted-proton density is modeled by a Gaussian or Fermi profile, the corresponding standard deviations are $\sigma_{\mathrm{G}} = 0.78$ or $\sigma_{\mathrm{F}} = 0.77$, respectively. Both values are substantially lower than the deviations reported for the Coulomb and proximity potential model ($\sigma_{\mathrm{CPPM}} = 1.075$), its deformed version for deformed nuclei ($\sigma_{\mathrm{CPPMDN}} = 1.275$), and the deformed two-potential approach ($\sigma = 1.253$), all evaluated with $S_p = 1$ [3, 8]. This indicates that, even at the baseline level, explicitly incorporating more realistic microscopic density information within the DPM framework leads to a significantly improved description of proton-radioactivity half-lives. However, the remaining deviations are still non-negligible. As indicated in Table 1, both density prescriptions tend to yield half-lives that are systematically smaller than the experimental values. This systematic underestimation originates from setting the preformation (spectroscopic) factor to unity ($S_p = 1$), which overestimates the probability of proton formation in the parent nucleus and leads to a systematic enhancement of the decay width.

To further improve the predictive power of the model, we explicitly include preformation factors in the subsequent calculations. The present DPM formulation cannot encode detailed nuclear-structure information such as shell effects, pairing, and deformation, and therefore, we adopt state-dependent spectroscopic factors calculated within RMF theory combined with BCS pairing. We use the microscopic spectroscopic factors of Qian *et al*. (S_p^{QYB}) and Zhang *et al*. (S_p^{ZHF}) as input preformation factors for the corresponding nuclei. This choice enables the model to assimilate essential structure information while preserving the systematic calculability of the DPM. On this basis, for each of the two proton-density prescriptions (Gaussian and Fermi), we recompute the DPM half-lives by introducing the S_p^{QYB} and S_p^{ZHF} sets of preformation (spectroscopic) factors. The resulting half-lives are

summarized in Table 1, and the corresponding RMS deviations are reported in Table 2.

Table 2 indicates that, for the present data set of 39 proton emitters, the RMS deviations for the Gaussian and Fermi densities are 0.78 and 0.77, respectively, when $S_p = 1$ is used as the baseline. When the $S_p^{\rm QYB}$ preformation factors are included, the RMS value decreases to 0.57 (Gaussian) and 0.46 (Fermi), representing improvements of 26.9% and 40.3%, respectively, relative to the baseline. When the $S_p^{\rm ZHF}$ preformation factors are used, the standard deviations drop to 0.44 (Gaussian) and 0.37 (Fermi), corresponding to improvements of 43.6% and 51.9%, respectively, relative to their $S_p = 1$ baselines. These results confirm that the inclusion of state-dependent preformation factors, which embed nuclear-structure information, substantially enhances the DPM performance for both density prescriptions. The combination DPM(Fermi)+$S_p^{\rm ZHF}$ achieves $\sigma = 0.37$, which is smaller than the value of $\sigma = 0.443$ reported for the deformed two-potential approach that explicitly includes both deformation effects and spectroscopic factors [8]. This implies that the spectroscopic factors of Zhang *et al*. lead to the most pronounced improvement and appear to be more compatible with the present DPM framework at the global level.

In recent years, several modern microscopic or semi-microscopic studies of proton radioactivity systematics have been conducted. For example, Xu *et al*. [48] proposed an improved Gamow-type description by incorporating a screened Coulomb (Hulthen-like) barrier with two adjustable parameters and reported RMS deviations of 0.274 for 31 spherical emitters and 0.367 for 13 deformed emitters in $\log_{10} T_{1/2}$. Delion and Dumitrescu [49] investigated universal proton-emission systematics within a penetrability–formation factorization scheme and found that centrifugal and quadrupole-deformation contributions to the action are typically smaller than the Coulomb part; therefore, the global systematics can be described by an approximately universal trend within a factor-of-two accuracy. From a more fundamental viewpoint, Delion [50] further emphasized the factorization of the decay width into penetrability and reduced width and derived a nearly linear rule linking $\log_{10}\gamma^2$ to the fragmentation potential. Very recently, Ismail *et al*. [51] performed self-consistent HFB calculations with the Gogny D1S interaction to obtain deformed daughter densities and constructed folding potentials based on the M3Y-Paris interaction, achieving $\sigma \approx 0.41$ for a set of experimental proton emitters. In this context, the present DPM provides a complementary semi-microscopic route in which the barrier is generated from a double-folding potential using finite-size proton and daughter densities, while the nucleus-dependent structure effects are incorporated through microscopic RMF+BCS spectroscopic factors. The resulting global deviation $\sigma = 0.37$ for DPM(Fermi) plus $S_p^{\rm ZHF}$ indicates that an accurate barrier description combined with microscopic structure input is essential for a high-precision global reproduction of proton-emission half-lives.

To assess the performance of this preferred combination at the level of observables, Fig. 1 displays the residuals between the calculated and experimental half-lives, $\Delta \equiv \log_{10} T_{1/2}^{\rm cal} - \log_{10} T_{1/2}^{\rm exp}$. For the DPM calculations employing the Fermi proton density with $S_p^{\rm ZHF}$ preformation factors, the distribution is narrowly centered around zero, and the deviations for most nuclei satisfy $|\Delta| \lesssim 0.5$; the largest deviation is approximately $|\Delta| = 1.05$. The points marked by black arrows correspond to proton emission from isomeric states of a given nucleus. Except for ^{185}Bi^m, these isomeric emitters all lie within the ±0.5 band, indicating that, for given Q_p, J^π (and hence the minimum orbital angular momentum l), and S_p, the present DPM framework provides a good description of isomeric decays. For the remaining outlier ^{185}Bi^m, the positive residual (calculated half-life longer than experiment) can plausibly be attributed to the enhanced structure sensitivity near the $Z = 82$ shell closure, indicating a possible deformation or configuration mismatch between the parent and daughter nuclei, and the small S_p value tabulated for this state.

To further characterize possible structure-related trends, we perform a grouped analysis of the residuals according to the minimum orbital angular momentum l. In the present sample, the numbers of emitters with $l = 0, 2, 3, 5$ are $N_{l=0} = 8$, $N_{l=2} = 13$, $N_{l=3} = 3$, and $N_{l=5} = 15$, respectively, and the corresponding RMS deviations under the preferred DPM(Fermi)+$S_p^{\rm ZHF}$ setting are listed in Table 3. Although the precise ordering of the RMS values is affected by the limited statistics, in particular for $l = 3$ with only three emitters, the results confirm that both the centrifugal barrier and local structure of the emitting system (*e.g*., deformation, configuration mixing,

Table 2. RMS deviations σ between the calculated and experimental half-lives and relative improvements $\Delta\sigma/\sigma_{S_p=1}$ for different models.

	$S_p = 1$			$S_p^{\rm QYB}$			$S_p^{\rm ZHF}$		
	Gaussian	Fermi	UDLP	Gaussian	Fermi	MUDLP	Gaussian	Fermi	MUDLP
σ	0.78	0.77	0.45	0.57	0.46	0.35	0.44	0.37	0.28
$\Delta\sigma/\sigma_{S_p=1}$				26.9%	40.3%	22.2%	43.6%	51.9%	37.8%

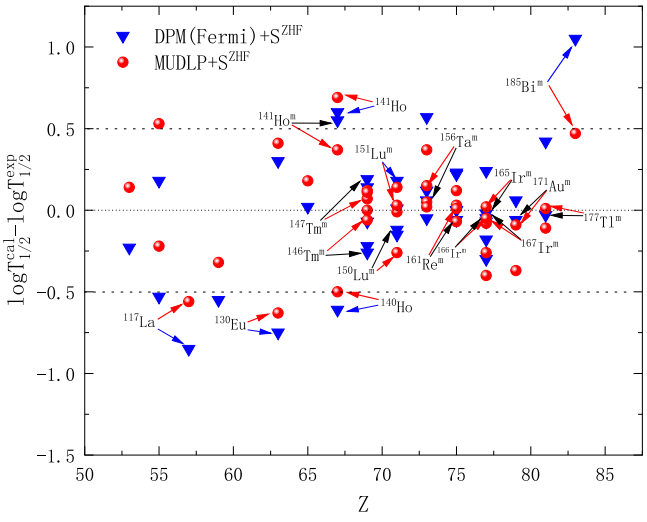

Fig. 1. (color online) Residual $\Delta = \log_{10} T^{\rm cal}_{1/2} - \log_{10} T^{\rm exp}_{1/2}$ for 39 proton emitters considered, comparing DPM(Fermi)+$S_p^{\rm ZHF}$ (triangles) and MUDLP+$S_p^{\rm ZHF}$ (circles).

Table 3. RMS deviations of Δ for different l groups.

l	5	3	2	0
N_l	15	3	13	8
RMS(Δ)	0.13	0.49	0.41	0.51

and pairing correlations as encoded in the RMF+BCS spectroscopic factors) play an important role in penetrability. Consequently, they influence the dispersion of the residuals. For the $l = 0$ and 2 subgroups, the centrifugal contribution to the barrier is relatively weak. Small variations in the decay energy Q_p and in the surface region of the double-folding potential, as well as local fluctuations in the microscopic spectroscopic factors $S_p^{\rm ZHF}$, induce comparatively large changes in the WKB action. Further, they are more strongly reflected in $\log_{10} T_{1/2}$, which naturally leads to the larger RMS deviations observed for these groups. In addition, these low-l emitters span a broad range of quadrupole deformations for both parent and daughter nuclei, and the associated structural heterogeneity is not explicitly encoded in the present DPM parametrization. In contrast, the $l = 5$ subgroup is dominated by decays assigned to well-defined high-j proton configurations, for which the adopted $S_p^{\rm ZHF}$ values are larger and exhibit smoother systematics in A and Z than those for the low-l emitters. The stronger centrifugal barrier reduces the relative impact of moderate uncertainties in Q_p and in the nuclear part of the potential. These features are consistent with the smaller RMS deviation obtained for $l = 5$. Finally, for nuclei with uncertain spin–parity assignments J^π, different plausible choices of l can lead to appreciable changes in the barrier height and WKB action. Therefore, the individual absolute residuals |Δ| may readily reach values of order 0.5–1.

Four ground-state proton emitters highlighted by blue arrows in Fig. 1, namely, ^{117}La, ^{130}Eu, ^{140}Ho (all with $\Delta < 0$, corresponding to overestimated widths and underestimated half-lives), and ^{141}Ho ($\Delta > 0$, underestimated width), are consistent with several sensitivity mechanisms summarized in the systematic studies of proton radioactivity. On the one hand, local variations of the preformation amplitude along an isotopic chain may not be fully captured by a global parametrization of S_p, and therefore, slight overestimates or underestimates of S_p are directly mapped onto corresponding over- or underpredictions of the decay width. On the other hand, moderate nuclear deformation and configuration mismatch between the parent and daughter nuclei can modify the effective shape of the inner part of the barrier (for example, the height and thickness of the potential wall) and thus influence the penetrability through the WKB action integral. Furthermore, in the relatively low-Q_p region, small changes in the double-folding interaction near the nuclear surface (e.g., through the surface diffuseness or the effective strength of exchange-related contributions) can induce noticeable modifications in the barrier profile. Such changes are exponentially amplified in the WKB action and can lead to sizable variations in penetrability, generating relatively large residuals for a few individual nuclei. Although a Gaussian density distribution is often considered more suitable for describing light spherical nuclei, under the present calibration, its performance for proton-radioactivity half-lives is systematically inferior to that of the two-parameter Fermi density. This likely reflects the fact that key surface parameters used in constructing the folding potential (such as radius and diffuseness) were originally tuned under the assumption of a Fermi-type density and are therefore not optimal for the Gaussian case. To further improve the Gaussian-based results, a dedicated refit of relevant parameters within the Gaussian-density assumption would be necessary. Motivated by the universal correlations between the decimal logarithm of half-lives and negative decimal logarithm of penetrability reported for α decay and cluster radioactivity [46, 52], we examine the systematics between the experimental half-lives and barrier penetrability for proton emission within the present DPM framework. We plot $\log_{10} T^{\rm exp}_{1/2}$ as a function of $-\log_{10} P$, where P is obtained from the WKB action integral using the DPM(Fermi) potential. As shown in Fig. 2, the data exhibit a clear near-linear global trend, supporting the applicability of a universal-type behavior to proton emission within our framework. The residual scatter can be attributed to nucleus-dependent structure effects encoded in S_p and to experimental uncertainties, which is consistent with the observation of Adel and Abdulghany that proton-decay systematics are more dispersed than those for α decay. Therefore, the observed near-linear systematics indicate that the DPM(Fermi) barrier provides a consistent global

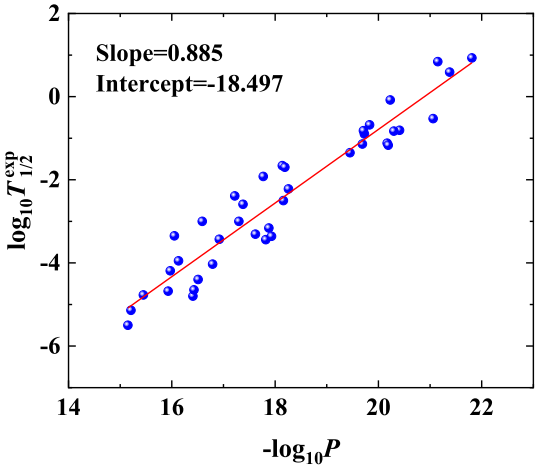

Fig. 2. (color online) $\log T_{1/2}^{\rm exp}$ versus $-\log_{10}P$ for the considered proton emitters, where P is the WKB penetrability calculated with the DPM(Fermi) potential.

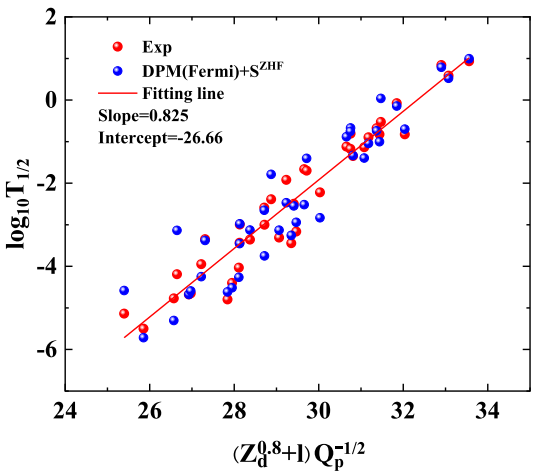

Fig. 3. (color online) Modified Geiger–Nuttall plot for proton radioactivity: $\log_{10}T_{1/2}$ as a function of $X=(Z_d^{0.8}+l)Q_p^{-1/2}$ (with Q_p in MeV). Red circles denote experimental half-lives, and blue circles denote the present DPM(Fermi)+$S_p^{\rm ZHF}$ results. The solid line is a linear fit to the experimental data.

description of the penetrability governing proton emission and can serve as a reliable baseline for systematic half-life studies. Building on the above penetrability–half-life correlation, we examine the modified Geiger–Nuttall (GN) systematics proposed by Chen *et al.* [37], which explicitly account for the daughter charge and angular-momentum dependence. We plot $\log_{10}T_{1/2}^{\rm exp}$ as a function of $X=(Z_d^{0.8}+l)Q_p^{-1/2}$ for all proton emitters considered in the present work. As shown in Fig. 3, the experimental half-lives exhibit an approximately linear trend in this modified GN representation. Our DPM(Fermi)+$S_p^{\rm ZHF}$ results follow the same global systematics and lie close to the experimental fitting line, indicating that the penetrabilities generated by the present DPM(Fermi) potential are consistent with the empirical modified GN behavior at the systematics level. The remaining deviations are attributed to nucleus-dependent structure effects encoded in S_p and to experimental uncertainties in Q_p and spin–parity assignments. Collectively, the present results indicate that, when a two-parameter Fermi proton density is employed in combination with the preformation (spectroscopic) factors of Zhang *et al.*, the DPM framework provides a quantitatively reliable description of nuclear proton radioactivity (with a global RMS of about 0.37 and most nuclei satisfying $|\Delta|\lesssim 0.5$). Further, it provides a good description of proton emission from isomeric states. This provides a solid basis for extending the model to half-life predictions in regions closer to and beyond the current proton drip line.

In parallel with the microscopic route, we fit an analytic UDLP to the same data set. When preformation effects are not included explicitly ($S_p=1$), the UDLP already achieves $\sigma=0.45$, which is better than the DPM baselines without preformation. When the $S_p^{\rm ZHF}$ spectroscopic factors are incorporated into UDLP, hereafter referred to as MUDLP, the dispersion is further reduced to $\sigma=0.28$, while the UDLP variant employing $S_p^{\rm QYB}$ yields $\sigma=0.35$ (see Table 2). The corresponding fitted coefficients for the original UDLP (with $S_p=1$) and for its MUDLP extension, whose parameters are obtained from a global fit including the microscopic spectroscopic factors $S_p^{\rm ZHF}$, are summarized in Table 4. The additional improvement achieved by MUDLP indicates that the analytic law can explicitly absorb slowly varying global systematic trends present in the data, including the near-linear dependence on $A_d^{1/3}$ or surrogate fragmentation-potential variables [7] commonly discussed in systematics studies. In contrast, in purely barrier-penetration-based models, such trends are typically only encoded implicitly through the combined effect of barrier parameters and the WKB action. Further, we plot the residuals obtained from MUDLP+$S_p^{\rm ZHF}$ in Fig. 1 and compare them with experimental results. As shown in Fig. 1, when going from DPM(Fermi)+$S_p^{\rm ZHF}$ to MUDLP+$S_p^{\rm ZHF}$, the data points contract more tightly around $\Delta=\log_{10}T_{1/2}^{\rm cal}-\log_{10}T_{1/2}^{\rm exp}=0$, and most nuclei fall within the $|\Delta|\leqslant 0.5$ band. More importantly, the same set of nuclei remain the most challenging cases in both approaches (although with smaller residuals under MUDLP), which suggests that these deviations are primarily constrained by common limitations of nuclear structure or input data, rather than by deficiencies specific to either model.

On the microscopic side, the inclusion of state-dependent preformation factors S_p is a key lever for significantly improving the predictive accuracy of the DPM. Under the present calibration, the combination DPM(Fermi)+$S_p^{\rm ZHF}$ achieves good global performance (with $\sigma=0.37$) and provides a physically transparent description of systematic differences between ground-state

Table 4. Adjustable parameter values of the UDLP and MUDLP formulas.

Model	a	b	c	d
UDLP	0.38	-0.52	-16.93	2.44
MUDLP	0.43	-0.64	-18.52	2.62

and isomeric decays. On the analytic side, the MUDLP+$S_p^{\rm ZHF}$ parametrization, which incorporates the same spectroscopic factors and smooth systematics, also achieves a small dispersion of $\sigma = 0.28$ for the same data set while highlighting the same set of structure-limited nuclei as the DPM results. Despite the smaller statistical dispersion achieved by MUDLP+$S_p^{\rm ZHF}$ on the present data set, this approach remains an empirical interpolation formula in nature, with a more simplified treatment of barrier shapes and nuclear-structure effects. Consequently, when extrapolating beyond the region of known nuclei, its physical controllability and robustness are more limited than those of the DPM framework, which is based on folded potentials and an explicit WKB tunneling picture. In view of these considerations, we adopt DPM(Fermi)+$S_p^{\rm ZHF}$ as the central estimator for subsequent half-life predictions and use MUDLP+$S_p^{\rm ZHF}$ for independent empirical validation and measurement of theoretical uncertainty. The two approaches yield mutually consistent descriptions of the known proton emitters, providing a robust theoretical basis for predicting proton-radioactivity half-lives of candidate nuclei beyond the present drip-line reach. On this basis, we employ both methods to predict the half-lives of several nuclei that are expected to exhibit proton radioactivity, providing useful guidance for future experimental investigations.

For several candidate nuclei near the proton drip line whose proton radioactivity has not yet been observed, we provide half-life estimates using three prescriptions that share the same microscopic spectroscopic factors $S_p^{\rm ZHF}$ but differ in their treatment of the barrier: the DPM with Fermi- and Gaussian-type proton densities and the analytic MUDLP formula. The adopted spins and parities of the parent and daughter nuclei are taken from NUBASE2020, while the decay energies Q_p are taken from AME2020; the spectroscopic factors are taken from Ref. [6]. For ^{104}Sb, whose spin–parity is not specified in NUBASE2020, the minimum orbital angular momentum carried by the emitted proton is taken as $l = 2$ following the configuration proposed in Ref. [6]. The corresponding values of $\log_{10} T_{1/2}$ are listed in Table 5. These estimates are conditional on the AME2020 Q_p values deduced from the available experimental mass data.

For each candidate nucleus, the three approaches yield mutually consistent results, with differences in $\log_{10} T_{1/2}$ typically on the order of 0.5 and not exceeding approximately 0.9. This spread may be considered a simple estimate of the present theoretical systematic uncertainty. The predicted half-lives cover a broad range of time scales, from sub-microsecond emitters such as ^{103}Sb and ^{169}Au to longer-lived cases such as ^{162,163}Re and ^{104}Sb. The largest model-to-model variation is found for ^{184}Bi, where the spread between the DPM and MUDLP predictions reaches nearly 0.9 in $\log_{10} T_{1/2}$. This enhanced sensitivity is likely associated with strong proton shell effects around the magic number $Z = 82$. Proton emission from ^{184}Bi populates this closed proton shell in the daughter nucleus, and the very small spectroscopic factor $S_p^{\rm ZHF} = 0.01$ makes the calculated width susceptible to modest changes in the barrier parametrization. Collectively, these predictions may serve as a useful guide for future experimental searches for new proton emitters in this mass region.

IV. SUMMARY AND CONCLUSIONS

In this study, we extended the DPM previously validated for α decay to the description of proton radioactivity in nuclei with $53 \leqslant Z \leqslant 83$. The nuclear interaction between the emitted proton and daughter nucleus was obtained by folding a Skyrme–type effective nucleon–nucleon interaction with finite–size proton densities and

Table 5. Conditional proton-emission half-life estimates for candidate proton emitters calculated with the DPM(Fermi) +$S_p^{\rm ZHF}$ and MUDLP formula. The input Q_p values are taken from AME2020 (deduced from available experimental mass data), and the remaining input quantities are listed.

Nucleus	Q_p/MeV	J_p^π	J_d^π	l	$S_p^{\rm ZHF}$	$\log_{10} T_{1/2}^{\rm th}$/s		
						Gaussian	Fermi	MUDLP
^{103}Sb	0.98	5/2+#	0+	2	1.00	−6.68	−6.97	−6.56
^{104}Sb	0.51	—	5/2+#	2 [6]	1.00	1.66	1.33	1.80
^{162}Re	0.79	(2)-	7/2-#	2	0.83	4.88	4.38	4.31
^{163}Re	0.72	1/2+	0+	0	0.92	5.67	5.39	5.06
^{169}Au	1.95	1/2+#	0+	0	0.32	−7.53	−7.76	−8.30
^{184}Bi	1.56	3+#	3/2-*	1	0.01	−2.05	−2.39	−2.94

spherical daughter densities. The half-lives were evaluated within the WKB approximation for 39 known proton emitters. Microscopic, state-dependent spectroscopic factors S_p^{QYB} and S_p^{ZHF} from RMF+BCS calculations were incorporated to consider the structural dependence of the proton preformation probability.

A systematic comparison with experimental half-lives showed that treating the proton as an extended object improved the overall agreement with data compared with the Coulomb-and-proximity-potential model and with the deformed two-potential approach when the preformation factor was neglected. The inclusion of microscopic spectroscopic factors provided the main leverage for further reducing the global RMS deviation, with the combination DPM(Fermi)+S_p^{ZHF} emerging as the preferred setting in the present framework and achieving $\sigma = 0.37$. In parallel, we constructed a modified UDLP (MUDLP) by introducing an explicit spectroscopic-factor term. The resulting analytic formula closely reproduced the DPM trends and reduced the dispersion to $\sigma = 0.28$ for the same data set.

To gain qualitative insight into structure-related trends, we analyzed the residuals grouped by the minimum orbital angular momentum l. The $l = 0$ and 2 subgroups displayed larger RMS deviations, which can be traced to the weaker centrifugal contribution to the barrier: small variations in Q_p, in the surface region of the double-folding potential, or in S_p^{ZHF} were more strongly amplified in the WKB action and in $\log_{10} T_{1/2}$. In contrast, the $l = 5$ subgroup, dominated by well-defined high-j configurations, showed a smaller dispersion. The largest model-to-model variation was found for ^{184}Bi, where strong proton shell effects around the magic number $Z = 82$ and very small spectroscopic factor $S_p^{\mathrm{ZHF}} = 0.01$ made the calculated width particularly sensitive to the details of the barrier.

Finally, we used the DPM(Fermi)+S_p^{ZHF} and MUDLP+S_p^{ZHF} prescriptions to predict proton-emission half-lives for several nuclei near the proton drip line whose proton radioactivity has not yet been observed. For each candidate, the two approaches yielded mutually consistent half-lives, with differences in $\log_{10} T_{1/2}$ remaining within approximately one order of magnitude and typically below ~ 0.9. Thus, our results demonstrate that the DPM supplemented with microscopic spectroscopic factors provides a reliable semi-microscopic framework for describing proton radioactivity and for extrapolating toward yet-unobserved proton emitters, while the MUDLP formula offers a compact analytic complement. These predictions may serve as a useful guide for future experimental searches in the vicinity of the proton drip line. We emphasize that the present extrapolations for candidate nuclei are conditional on the adopted AME2020 Q_p values; a fully predictive description, in which both Q_p and $T_{1/2}$ are obtained self-consistently, would require coupling to nuclear-mass models or microscopic resonance approaches, which will be pursued in future work.

References

[1] K. Jackson, C. Cardinal, H. Evans *et al.*, Phys. Lett. B **33**, 281 (1970)
[2] J. Cerny, J. Esterl, R. Gough *et al.*, Phys. Lett. B **33**, 284 (1970)
[3] K. P. Santhosh and I. Sukumaran, Phys. Rev. C **96**, 034619 (2017)
[4] M. Karny, K. Rykaczewski, R. Grzywacz *et al.*, Phys. Lett. B **664**, 52 (2008)
[5] C. Qi, D. S. Delion, R. J. Liotta *et al.*, Phys. Rev. C **85**, 011303 (2012)
[6] H. F. Zhang, Y. J. Wang, J. M. Dong *et al.*, J. Phys. G: Nucl. Part. Phys. **37**, 085107 (2010)
[7] J. L. Chen, X. H. Li, X. J. Wu *et al.*, Eur. Phys. J. A **57**, 305 (2021)
[8] D.-M. Zhang, L. J. Qi, H. F. Gui *et al.*, Phys. Rev. C **108**, 024318 (2023)
[9] Y. Fan, X. D. Sun, L. J. Liao, X. Liu *et al.*, Phys. Rev. C **112**, 054311 (2025)
[10] J. L. Chen, J. H. Cheng, J. G. Deng, *et al.*, Nuclear Physics Review **35**(3), 257 (2018)
[11] S. Åberg, P. B. Semmes, and W. Nazarewicz, Phys. Rev. C **56**, 1762 (1997)
[12] D. Delion, R. Liotta, and R. Wyss, Physics Reports **424**, 113 (2006)
[13] C. N. Davids and H. Esbensen, Phys. Rev. C **64**, 034317 (2001)
[14] B. Barmore, A. T. Kruppa, W. Nazarewicz *et al.*, Phys. Rev. C **62**, 054315 (2000)
[15] M. Balasubramaniam and N. Arunachalam, Phys. Rev. C **71**, 014603 (2005)
[16] J. M. Dong, H. F. Zhang, W. Zuo *et al.*, Chin. Phys. C **34**, 182 (2010)
[17] D. N. Basu, P. R. Chowdhury, and C. Samanta, Phys. Rev. C **72**, 051601 (2005)
[18] B. Sahu, S. K. Agarwalla, and S. K. Patra, Phys. Rev. C **84**, 054604 (2011)
[19] Y. B. QIAN, Z. Z. REN, and D. D. NI, Chin. Phys. Lett. **27**, 072301 (2010)
[20] Y. Qian and Z. Ren, Eur. Phys. J. A **52**, 68 (2016)
[21] A. Zdeb, M. Warda, C. Petrache *et al.*, Eur. Phys. J. A **52**, 323 (2016)
[22] J. L. Chen, X. H. Li, J. H. Cheng *et al.*, J. Phys. G: Nucl. Part. Phys. **46**, 065107 (2019)
[23] D. M. Zhang, X. Y. Hu, L. J. Qi *et al.*, Chin. Phys. C **48**, 044102 (2024)
[24] N. Teruya, S. B. Duarte, and M. M. N. Rodrigues, Phys. Rev. C **93**, 024606 (2016)
[25] C. Guo and G. Zhang, Eur. Phys. J. A **50**, 187 (2014)
[26] D. M. Zhang, L. J. Qi, D. X. Zhu *et al.*, Nucl. Sci. Tech **34**, 55 (2023)
[27] A. Soylu, F. Koyuncu, G. Gangopadhyay *et al.*, Chin. Phys.

C **45**, 044108 (2021)
[28] J. G. Deng, X. H. Li, J. L. Chen *et al*., Eur. Phys. J. A **55**, 58 (2019)
[29] H. Yang, X. Li, X. Song *et al*., Phys. Rev. C **113**, 014307 (2026)
[30] J. Patterson and R. Peterson, Nucl. Phys. A **717**, 235 (2003)
[31] J. Zhang, X. Tu, Y. Huang *et al*., Comput. Phys. Commun. **312**, 109587 (2025)
[32] M. Park, Y. Choi, and Y. Kim, Int. J. Mod. Phys. E **34**, 2550021 (2025)
[33] Z. Yuan, D. Bai, Z. Wang *et al*., Sci. Chin. Phys., Mech. Astron. **66**, 222012 (2023)
[34] J. M. Dong, H. F. Zhang, and G. Royer, Phys. Rev. C **79**, 054330 (2009)
[35] Y. Lim, X. Xia, and Y. Kim, Phys. Rev. C **93**, 014314 (2016)
[36] Q. Zhao, J. M. Dong, J. L. Song *et al*., Phys. Rev. C **90**, 054326 (2014)
[37] J. L. Chen, J. Y. Xu, J. G. Deng *et al*., Eur. Phys. J. A **55**, 214 (2019)
[38] Z. X. Zhang and J. M. Dong, Chin. Phys. C **42**, 014104 (2018)
[39] V. Dehghani and S. Alavi, Chin. Phys. C **42**, 104101 (2018)
[40] J. Dong, W. Zuo, J. Gu *et al*., Phys. Rev. C **81**, 064309 (2010)
[41] M. R. Pahlavani and F. Ahmadvand, Int. J. Mod. Phys. E **32**, 2350036 (2023)
[42] G. G. Adamian, N. V. Antonenko, R. V. Jolos *et al*., Int. J. Mod. Phys. E **5**, 191 (1996)
[43] W. Yahya and B. Falaye, Nucl. Phys. A **1015**, 122311 (2021)
[44] F. G. Kondev, M. Wang, W. J. Huang *et al*., Chin. Phys. C **45**, 030001 (2021)
[45] M. Wang, W. J. Huang, F. G. Kondev *et al*., Chin. Phys. C **45**, 030003 (2021)
[46] A. Adel and A. R. Abdulghany, Physica Scripta **96**, 125314 (2021)
[47] M. Pahlavani and S. Rahimi Shamami, Chinese Journal of Physics **66**, 733 (2020)
[48] Y.-Y. Xu, X.-Y. Hu, D.-X. Zhu *et al*., Nucl. Sci. Tech **34**, 30 (2023)
[49] D. S. Delion and A. Dumitrescu, Phys. Rev. C **103**, 054325 (2021)
[50] D. S. Delion, Phys. Rev. C **80**, 024310 (2009)
[51] M. Ismail, A. Adel, A. Y. Ellithi *et al*., Chin. Phys. C **50**, 1 (2026)
[52] D. N. Poenaru, R. A. Gherghescu, and W. Greiner, Phys. Rev. C **83**, 014601 (2011)